



## A complex network based approach for knee Osteoarthritis detection: Data from the Osteoarthritis initiative



Lucas C. Ribas<sup>a,d,\*</sup>, Rabia Riad<sup>b</sup>, Rachid Jennane<sup>c</sup>, Odemir M. Bruno<sup>a,d</sup>

<sup>a</sup> Institute of Mathematics and Computer Science, University of São Paulo, Avenida Trabalhador São-Carlense, 400, Centro, 13566-590 São Carlos, SP, Brazil

<sup>b</sup> ERMAM FPO, Ibn Zohr University, Ouarzazate 45000, Morocco

<sup>c</sup> IDP Laboratory, UMR CNRS 7013, University of Orléans, Orléans 45067, France

<sup>d</sup> São Carlos Institute of Physics, University of São Paulo, PO Box 369, 13560-970 São Carlos, SP, Brazil

### ARTICLE INFO

#### Keywords:

Texture analysis  
Networks  
Feature extraction  
OsteoArthritis detection

### ABSTRACT

OsteoArthritis (OA) is a joint disease caused by cartilage loss in the joint and bone changes. Early knee OA prediction based on bone texture analysis is a difficult task in medical image analysis. This paper presents a new approach based on concepts of complex network theory to extract texture features related to OA from radiographic knee X-ray images. An X-ray image is modeled into a complex network mapping each pixel into a node and connecting two nodes based on a given Euclidean distance. Then, a set of thresholds is applied to remove some edges and reveal texture properties. Our proposed model employs a specific strategy to automatically select the set of thresholds. A new set of statistical measures extracted from the network are used to compute a feature vector evaluated in a classification experiment using knee X-ray images from the OsteoArthritis Initiative (OAI) database. Our proposed approach is compared to state-of-the-art learning models (AlexNet, VGG, GoogleNet, InceptionV3, ResNet, DenseNet and EfficientNet) as well as to different traditional texture descriptors. Results show that the proposed method is competitive and is potentially promising for early knee OA detection.

### 1. Introduction

OsteoArthritis (OA) is a degenerative disease that causes pain, inflammation, and dysfunctions in joints [1,2]. It affects mostly knees, hips, and hands, which makes it the major cause of the mobility limitation and physical disability after the age of 50 years [3,4]. Knee OA is characterized by cartilage degradation, reduction of joint space width as well as osteophytes formation but also changes of bone architecture [3]. A manual classification has been developed by Kellgren and Lawrence (K&L) dividing the OA into five stages of severity (normal (grade 0), doubtful (grade 1), minimal (grade 2), moderate (grade 3) and severe (grade 4)). Grade 0 indicates the definite absence of OA and grade 2 early OA [5]. K&L classification score is based on radiological features such as narrowing of joint cartilage and osteophytes formation [5]. Several studies have underlined that characterizing the texture of the trabecular bone on X-ray images could have a good performance to predict knee OA before reduction of the joint width and osteophyte formation [6,7]. Consequently, trabecular bone (TB) characterization is increasingly used in the assessment of trabecular bone changes due to OA [4,8–10]. Several imaging modalities have been used to acquire the TB images, such as magnetic resonance imaging (MRI), X-ray imaging

and scintigraphy. The current gold standard for diagnosing knee OA, is X-ray imaging (plain radiography). Due in particular to its safety, wide availability, low cost, acquired images are readily understood, and the trabecular bone texture obtained on the X-ray images is related to the three-dimensional bone micro-architecture [3,9].

In the literature, several texture analysis methods have been developed to analyze the TB structure on X-ray images [8,9,11]. Shamir et al. [8] used various methods (e.g., multiscale histograms, Haralick textures and Fourier transforms) to extract features from the X-ray images. On a dataset of 193 X-ray images, an accuracy of 80.4% was obtained using a weighted nearest neighbor classifier. In [9], using a rotation invariant method of Signature Dissimilarity Measure (SDM), authors reached an accuracy of 78.8% on a dataset of 137 X-ray images. Riad et al. [11] proposed a texture analysis method based on complex Wavelet decomposition. Using 688 X-ray images, authors obtained an accuracy of 80.38%. In [10], Janvier et al. used the Hurst parameter for OA progression. A dataset of 1124 knee X-ray patients was used to collect several regions of interests (ROIs) for texture analysis and OA classification. An AUC (Area Under the Curve) of 0.73 was obtained when combining the Hurst parameter to Joint Space Narrowing and clinical covariates. In [7], several ROIs were extracted from a set of 688 knee X-

\* Corresponding author.

ray images and processed using fractal analysis to evaluate whether TB features could predict OA initiation. An AUC of 0.71 was obtained when combining tibial osteophytes and fractal features. Despite the promising performance obtained by these recent techniques, most of them have at least one of the following drawbacks: high computational complexity [8], using a global method based on similarity patterns [9], and the size of the datasets used in these studies are also questionable [8,9].

With the evolution of deep neural network architectures, new strategies are emerging for image classification [12,13]. Many deep learning models have been developed to diagnose knee OA severity. Anthony et al. [14,15] employed a Fully-Convolutional Network (FCN) based method to localize knee joints, and used a deep Convolutional Neural Network (CNN) to classify the different stages of knee OA severity. Tiulpin et al. [16] proposed another method based on Deep Siamese CNNs to score knee OA severity according to KL grading scale automatically. All these studies [14–16] treated knee OA issue as a multi-class problem and focused on the various classes based on KL grades. More recently, from our group, Nasser et al. [17] focused on early detection of knee OA (grade 0 for non-OA, considered as controls vs. grade 2 for minimal OA). A new Discriminative Regularized Auto-Encoder (DRAE) for early detection of Knee OA was introduced. The DRAE consists of a combination of a discriminative loss function with the standard Auto-Encoder training criterion to improve knee OA detection.

In the present study, we introduce an approach based on the concept of complex networks (CNs) to model and characterize knee X-ray images for OA detection. Complex network analysis has been used with success in different problems of image analysis [18–20]. In the proposed approach, firstly, each image is modeled as a complex network representing each pixel as a vertex and connecting two vertices according to a given Euclidean distance [21]. Then, thresholds are applied over the network edges to transform a regular network into another CN that highlights different properties of the image. We define these threshold values with an automatic selection strategy based on a Gaussian distribution modeling. Finally, different feature vectors with various statistical measures are computed from the built networks. As we are interested in early knee OA prediction, the resulting feature vector is used in a classification task to distinguish between X-ray images of normal knee (K&L grade 0) and minimal OA (K&L grade 2). Subjects with doubtful OA (K&L = 1) were removed to focus on healthy at risk patients. We did not consider grades 3 and 4 for severe knee OA because they are not compatible with the purpose of early detection. Also, to be comparable with the following studies [7,11,22], only grades 0 and 2 were considered. For experiments, we used 688 knee images (344 from control subjects and 344 from OsteoArthritis Patients) collected from the OsteoArthritis Initiative (OAI) database [23].

The remainder of the paper is structured as follows. Section 2 presents the concepts of networks and introduces our method to compute a feasible feature vector for knee OA classification. Then, Section 3 describes the database and the regions of interest. The proposed method is evaluated and the results are presented and discussed in Section 4. Section 5 concludes the paper.

## 2. Proposed approach

### 2.1. Complex network representation

Formally, an undirected weighted complex network is represented by a pair  $C = (V, E)$ , where  $V$  is a set of vertices  $v$  and  $E$  is a set of edges  $e_{v,v'}$ . The weight of the edge between vertices  $v$  and  $v'$  is given by  $w(e_{v,v'})$ . The research in CNs comprises two main steps: modeling of the data as a CN and its topological analysis through a set of measurements ([21,24,25]). By this set of measurements, it is possible to characterize and classify different complex network topologies.

The main and simplest measures from complex networks are the

vertex degree and vertex strength. The definition of the degree  $k(v)$  of a CN vertex  $v$  is given by the number of edges linked to  $v$ , according to

$$k(v) = \sum_{v' \in V} \begin{cases} 1, & e_{v,v'} \in E \\ 0, & \text{otherwise.} \end{cases} \quad (1)$$

Using the degrees of the network vertices  $v \in V$  it is possible to obtain the degree histogram  $h$ , which is yielded as:

$$h(i) = \sum_{v \in V} \begin{cases} 1, & k(v) = i \\ 0, & k(v) \neq i. \end{cases} \quad (2)$$

The histogram is an accurate and simple representation which provides relevant statistical information of the network structure. Through the degree histogram, many features based on first-order statistics may be computed. The statistics features are calculated from the probability density function  $\rho(i)$  of the degree histogram  $h(i)$ , according to

$$\rho(i) = \frac{h(i)}{\sum_{i=0}^k h(i)} i = 0, 1, 2, \dots, k. \quad (3)$$

### 2.2. Image as complex network

Image acquisition is in major part responsible for the generation of unnecessary information. In the process of X-ray acquisition, pixel resolution is linked to electronic reading time. Longer is the acquisition, more accurate is the measurement. However, this is not compatible with life. Moreover, X-ray diffusion generates different artifacts and blur data. To maximize the entropy of the image and keep the essential information, a reduction of gray levels provides better and more easily exploitable images that are better suited for bone texture analysis. Without losing any generality, as our images are 16 bits (65536 gray-levels), a quantization to 8 bit (256 gray-levels) is achieved. To accomplish this, the gray-level intensity of each pixel  $p$  is converted.

Consider an image  $I$  as a pair  $(P, \Upsilon)$  where  $P$  is a set of pixels  $p = (x, y) \in P$  and  $\Upsilon$  is a mapping that assign to each pixel  $p = (x, y) \in P$  a gray-level intensity  $\Upsilon(p) \in [0, L]$  as follows:

$$\Upsilon(p) = \frac{\Upsilon(p) - \min(\Upsilon)}{\max(\Upsilon) - \min(\Upsilon)} * 255 \quad (4)$$

where  $\max(\Upsilon)$  and  $\min(\Upsilon)$  are the maximum and minimum gray-level intensities of the image, respectively.

To model an image as a complex network  $C$ , we adopted a methodology based on previous works [21,26]. Each pixel  $p$  is represented by a vertex  $v$  and two vertices  $v$  and  $v'$  are connected by a weighted edge  $e = (v, v') \in E$  if the Euclidean distance between their corresponding pixels is lower or equal than a given radius  $r$ , as follows:

$$E = \{e = (v, v') \in E | \sqrt{(x - x')^2 + (y - y')^2} \leq r\}. \quad (5)$$

**Fig. 1** shows an example of a textured image modeled as a regular complex network using  $r = \sqrt{2}$ . The edge weight  $\omega(v, v')$  is defined by the absolute difference of intensities between the two pixels that represent the vertices [21], as expressed by:

$$\omega(v, v') = \frac{(x - x')^2 + (y - y')^2 + r^2 |\Upsilon(p) - \Upsilon(p')|}{r^2 + r^2}, \forall e = (v, v') \in E, \quad (6)$$

where  $L$  is the maximum gray-level value.

Given a regular network, in order to obtain a complex behavior and highlight texture properties of the trabecular bone, a transformation was applied over the network. The last consists of removing edges whose weight is higher than a threshold value  $t$ , leading to a new set of edges,

$$E_t = \{e = (v, v') \in E | \sqrt{(x - x')^2 + (y - y')^2} \leq r \text{ and } \omega(v, v') \leq t\}. \quad (7)$$

This transformation may be understood as a multi-scale CN analysis

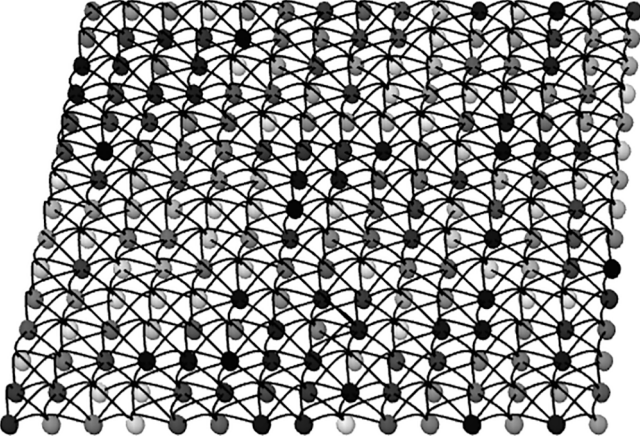


**Fig. 1.** Example of a texture image modeled as a regular network with a radius  $r = \sqrt{2}$ .

[24]. For small values of  $t$  (Fig. 2(a)), a network modeling small details (small set of pixels) in the image is obtained. Unlike, for high values of  $t$  (Fig. 2(c)), global details are modeled by the network. Fig. 2 illustrates this transformation for different values of the threshold  $t$ . As can be seen, when the value of  $t$  is decreased, more edges are removed (ie. edges with high weight) and only homogeneous regions (ie. edges with low weight) are kept connected.

While different existing methods in the literature suffer from image transformations such as rotation, our method is invariant to rotations and multi-scale analysis. The network modeling considers only the distance between pixels to create the network. Thus, regardless of the rotation, the topology of the network will be the same. Moreover, the use of different values for radius and threshold enables multi-scale analysis of the image. While small values of the radius and threshold characterize micro texture patterns, high values characterize macro texture patterns.

### 2.3. Signature

For the characterization of the network, the probability density function  $\rho(i)$  of the vertex degree is considered. The following features were computed: the mean, the variance and the Kurtosis as well as the entropy as a measure of the irregularity of the texture and the Inverse Difference Moment (IDM) as a measure of the homogeneity of the texture.

- Mean:

$$\phi = \sum_{i=0}^k i\rho(i) \quad (8)$$

- Entropy:

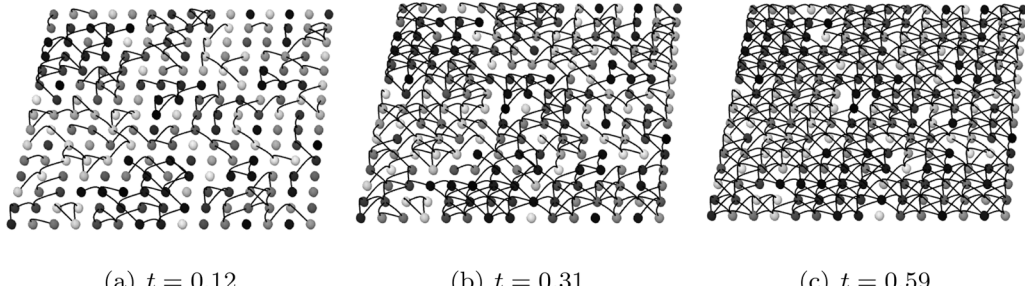


**Fig. 2.** Effects of different values of threshold  $t$  in a regular network. (a) For small values of  $t$ , small details are modeled, (c) as the value of  $t$  is increased, global details are modeled (ie. more heterogeneous regions are connected).

$$H = - \sum_{i=0}^k \rho(i) \log_2[\rho(i)] \quad (9)$$

- Variance:

$$\nu = \sum_{i=0}^k \rho(i)(i - \mu)^2 \quad (10)$$

- Kurtosis:

$$\kappa = \frac{\sum_{i=0}^k \rho(i)(i - \mu)^4}{\sigma^4} \quad (11)$$

- Inverse Difference Moment (IDM):

$$d = \sum_{i=0}^k \frac{1}{i^2 + 1} \rho(i) \quad (12)$$

These measures are computed over a network built with a radius  $r$  and a threshold  $t$ . In order to obtain a multiscale CN analysis, the mean feature  $\phi_t$  is computed for various values of  $t$ . The values of  $t$  are in a set of threshold  $\{t_0, t_1, \dots, t_n\}$  that is defined by an initial threshold value  $t_0$ , a final value  $t_n$  and the number of thresholds  $n$ . Therefore, a feature vector  $\Psi_r^\phi$  is constructed by concatenating features  $\phi_t$  using several values of  $t$ ,

$$\Psi_r^\phi = [\phi_{t_0}, \phi_{t_1}, \dots, \phi_{t_n}] \quad (13)$$

This feature vector contains temporary characteristics of the network according to the value of the threshold, which is tuned during the classification task. Then, we consider a feature vector  $\Upsilon_\phi$  that combines the feature vectors  $\Psi_r^\phi$  for different values of the radius  $r$ ,

$$\Upsilon_\phi = [\Psi_{r_1}^\phi, \Psi_{r_2}^\phi, \dots, \Psi_{r_m}^\phi] \quad (14)$$

Following the steps above, for each network measure, a feature vector is constructed as: mean  $\Upsilon_\phi$ , entropy  $\Upsilon_H$ , variance  $\Upsilon_\nu$ , kurtosis  $\Upsilon_\kappa$ , IDM  $\Upsilon_d$ . Finally, a final feature vector combining different network features is computed. In Section 4.2, different experiments are performed in order to identify the best combination of the network features.

### 2.4. Automatic threshold selection

Many methods based on complex networks present as a limitation the number of parameters used to build the set of thresholds,  $T$ . As described in Section 2.3, this set is defined by an initial threshold  $t_0$ , a final threshold  $t_n$ , and a number of thresholds  $n$ . In [21], the authors evaluated empirically these three parameters for different databases.

In order to define the set of thresholds, we employed an approach inspired from [27], which is based on modeling a Gaussian distribution of the edges of the set of training images. Compared to other techniques in the literature, the main advantage of the proposed approach is the automatic definition of the threshold. Initially, the complex network  $C = (V, E)$  is built for each image  $I \in Z$ , where  $Z$  is the set of training images of size  $|Z|$ . In this work, the set  $Z$  is composed of 10% of the samples of each class. At this step, the edges' weights of all  $|Z| * |E|$  connections are computed, while the threshold cutting over the network edges is not yet applied. Once the edges' weights are computed, the mean  $\mu$ , and standard deviation  $\sigma$ , for all training images in  $Z$  are estimated as follows:

$$\mu = \frac{1}{|Z| * |E|} \sum_{I \in P} \sum_{(v, v') \in E_I} \omega(v, v') \quad (15)$$

$$\sigma = \sqrt{\frac{1}{|Z| * |E|} \sum_{I \in P} \sum_{(v, v') \in E_I} (\omega(v, v') - \mu)^2} \quad (16)$$

Using the three-sigma rule and these two measures, it is possible to define the initial and final threshold values that ensure a minimum coverage of the edges' weights distribution, as follows:

$$\begin{aligned} t_0 &= \mu - \alpha\sigma \\ t_n &= \mu + \alpha\sigma. \end{aligned} \quad (17)$$

The parameter  $\alpha$  regulates the covering rate of the distribution. In this way,  $\alpha = 1$  covers approximately 68.27% of the distribution. On the other hand,  $\alpha = 3$  covers approximately 99.73%. Thus, it is possible to define the set of thresholds  $\{t_0, t_1, \dots, t_n\}$  for the whole database automatically by adjusting only  $\alpha$  and the number of thresholds  $n$ .

### 3. Data

#### 3.1. Patients

The data used in this paper was obtained from the OsteoArthritis Initiative (OAI) database (available at [23]), which was developed to investigate knee health in patients at chance for knee OA [28]. The study selected only computed radiography (CR) to avoid digitizing problems, and the different populations were divided based on K&L grades. As mentioned previously, the present work is focused on the early detection of knee OA. Thus, only K&L grade 0 and 2 were considered for severe OA, while grades 1, 3, and 4 were not used due to they are not compatible with the early detection task. Thus, in this study, only K&L grade 0 and 2 were considered. Radiographs with K&L grade 0 were considered as normal knee or Control Cases (CC) and radiographs with K&L grade 2 were considered as OsteoArthritis Patients (OP). Consequently, 688 knee radiographs were used (344 from CC subjects and 344 from OP subjects).

#### 3.2. Regions Of Interest (ROI)

A semi-automatic approach was employed to obtain the trabecular bone ROIs. First, four anatomical markers as shown in Fig. 3 were defined manually by a trained operator. Then, the tibial edge was calculated with the geodesic distance as the brightest path going through these anatomical markers [10]. Finally, an ROI of  $128 \times 128$  pixels was placed in the tibial region under the cortical bone (tibial edge) and the horizontal adjustment was determined as the center between extremities. Fig. 4 shows two examples of ROIs (CC and OP) which are modeled as networks in Fig. 5. For visualization purpose, the image size is  $32 \times 32$  pixels. For each extracted ROI, a network with specific characteristics of the K&L grade is generated. As can be seen, the regions more homogeneous of the ROIs are more connected in the network while the border regions are disconnected. This shows that the complex network topology reflects the main characteristics of the

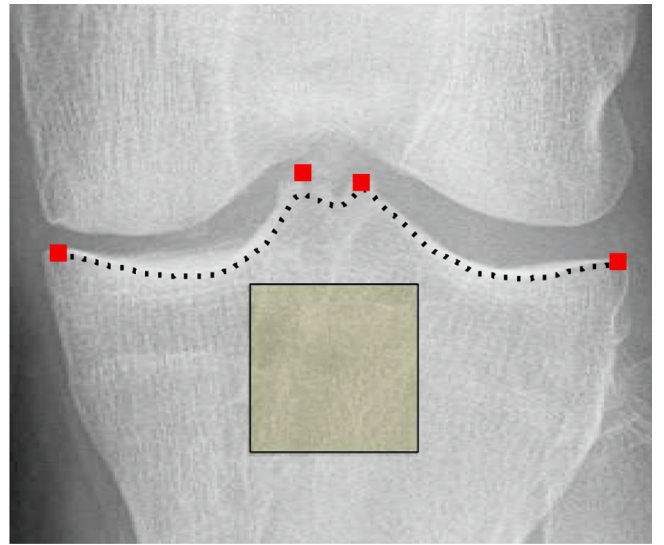


**Fig. 3.** Segmented Knee using a semi-automatic method. Red dots represent the anatomical markers manually defined. The dashed line represents the tibial edge.

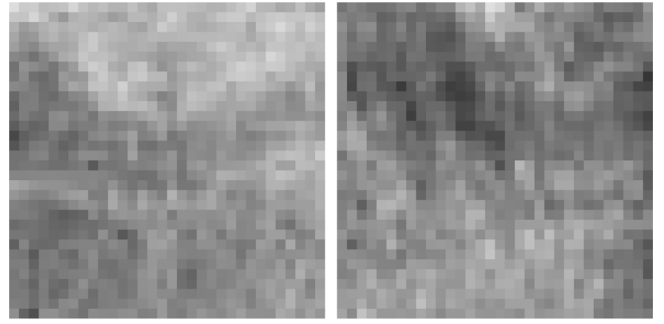


**Fig. 4.** Example of ROI images for K&L grade 0 (CC) and K&L grade 2 (OP).

images.

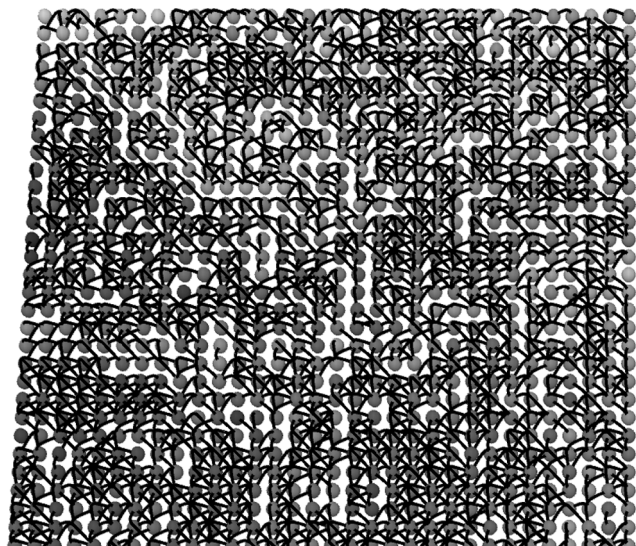
### 4. Results and discussion

#### 4.1. Experimental setup

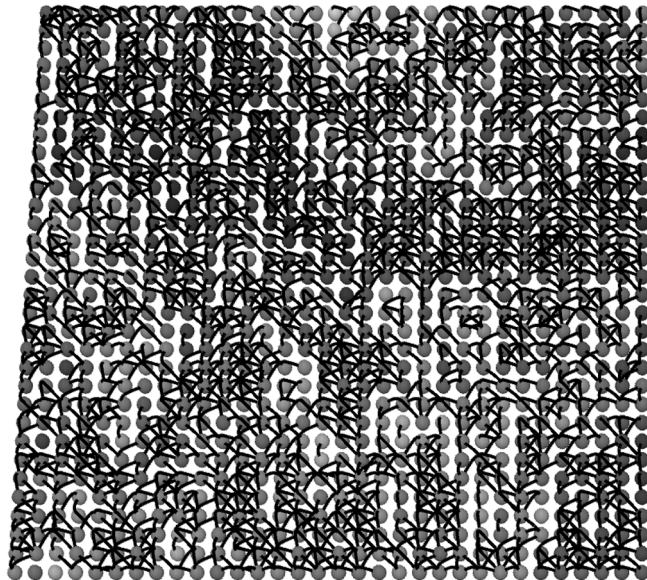
To perform the experiments, 344 CC X-ray images (CC) and 344 OP X-ray images (OP) were considered. In the experiments, we adopted three classifiers: the Support Vector Machine (SVM) with a linear kernel, k-Nearest Neighbors (k-NN) with the Euclidean distance and  $k = 9$  and the Linear Discriminant Analysis (LDA). Parameters and configurations were optimized to make the classifiers work optimally. To evaluate our approach, the leave-one-out cross-validation scheme was adopted. It consists of separating in each trial one sample from a given class for testing, while the remaining samples are used for supervised training. This process was repeated using all  $N$  samples to test. As a performance measure of this scheme, we used the accuracy  $A = \frac{C}{N}$  in which  $C$  is the number of samples correctly classified. We also computed the sensitivity and the specificity to measure the ability of the method to correctly detect positive and negative cases, respectively.

#### 4.2. Parameter analysis

In this section, the parameters of the proposed complex network and



(a) CC

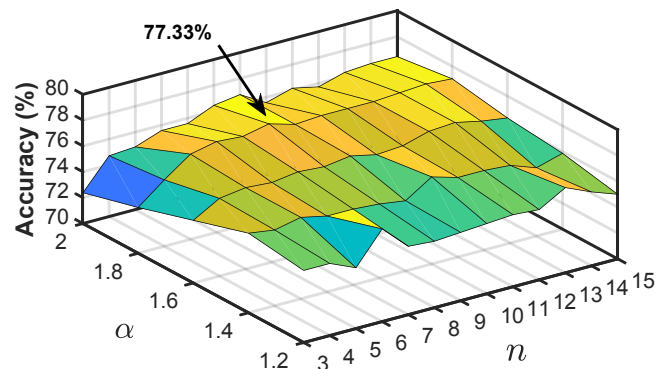


(b) OP

**Fig. 5.** ROI images shown in Fig. 4 modeled as complex networks.

their impact on knee OA prediction are analysed. These parameters are: the set of radiiuses  $R = \{r_0, r_1, \dots, r_m\}$  and the set of thresholds  $T = \{t_0, t_1, \dots, t_n\}$ . To investigate their influence, only the mean feature  $\phi$  is considered in the classification. The performance of the statistical measures used to characterize the network are also analyzed.

First, in order to define the set of thresholds  $T$ , the initial and final thresholds ( $t_0$  and  $t_n$ ) are computed according to the automatic threshold selection approach described in Section 2.4. To evaluate Eq. (17), we used values of  $\alpha$  varying from 1.2 to 2 by step of 0.2. Fig. 6 shows estimated accuracy rates as function of  $\alpha$  and the number of thresholds  $n$  using the SVM classifier. As can be seen, low values of  $\alpha$  produce low accuracy rates, while increasing the value of  $\alpha$  increases accuracy rates. Such behavior was expected: larger is  $\alpha$ , larger is the difference between the thresholds. Consequently, features obtained for each threshold are not similar to each other. The highest accuracy rates were obtained with

**Fig. 6.** Accuracy rate for different values of  $\alpha$  and  $n$  using the SVM classifier.

$\alpha = 1.8$ . Thus, using  $\alpha = 1.8$ , the corresponding threshold interval is  $[0.0012, 0.5808]$  ( $t_0 = 0.0012, t_n = 0.5808$ ).

Concerning the number of thresholds  $n$ , the set of thresholds  $T$  was divided into  $n$  equidistant values between  $t_0$  and  $t_n$ . Fig. 6 shows obtained accuracy rates by varying  $n$  from 3 to 15 for different values of  $\alpha$ . As can be seen, accuracy rates tend to increase when  $n$  is increased. This occurs because large values of  $n$  enlarge the size of the feature vector. However, larger feature vectors may not always guarantee better relevant features in terms of recognition and classification. Setting  $n = 9$  seems to be a good compromise for a high accuracy.

We also evaluated the combination of feature vectors  $\Psi_r^\phi$  for several values of the radius  $r$ . As Table 1 shows, the highest accuracy rate is obtained using  $r = \{1, 2, 3\}$ . Results also show that the performance is improved when the radius is increased from  $r = \{1\}$  to  $r = \{1, 2, 3\}$ . Then the accuracy becomes constant with more combinations. A higher value of  $r$  models a more dense CN, i.e., connects more distant vertices to each other, capturing global information of the texture. This suggests that local information are more relevant in terms of classification than global ones. This is consistent with our expectations as we are investigating the trabecular bone texture for knee OA prediction.

As the appropriate sets of thresholds and radiiuses were defined, we decided to study the influence of the statistical measures used to characterize the network. In this experiment, we also evaluated three different classifiers: the SVM, the k-NN (with  $k = 9$ ) and the LDA. Table 2 shows obtained accuracies for different statistical measures and their combinations using the three classifiers. As can be seen, the SVM achieved the highest accuracies in most cases when compared to the other classifiers. Results also show that when considered individually, kurtosis features have the highest capacity to discriminate a CN and thus knee OA patterns. When the different features are combined two-by-two, the highest accuracy is obtained using the variance and the entropy (80.81% in both classifiers SVM and LDA). On the other hand, when three features are combined, the best result is achieved with variance, kurtosis and IDM. However, the best accuracy was achieved when the mean, variance, kurtosis and IDM features are combined (81.40% using the SVM classifier). Compared to the other combinations, this combination produces the highest accuracy with a smallest number of features.

**Table 1**

Obtained accuracies for different combinations of the radius using the mean feature  $\phi$  and the SVM classifier.

Radius	Number of features	Accuracy (%)
{1}	10	77.33
{1,2}	20	78.20
{1,2,3}	30	78.34
{1,2,3,4}	40	78.34
{1,2,3,4,5}	50	78.34

**Table 2**

Obtained results using the proposed approach for different feature vectors and their combination using the best configuration defined in [Table 1](#) and the three classifiers.

Combined features					N. of features	Accuracy rate (%)		
Mean	Variance	Kurtosis	Entropy	IDM		SVM	k-NN	LDA
X					30	78.34	76.45	78.77
	X				30	78.20	78.34	79.79
		X			30	78.92	78.05	78.48
			X		30	77.76	76.45	79.36
				X	30	78.05	77.90	78.77
X	X				60	77.33	77.90	79.36
X		X			60	80.38	76.74	80.08
X			X		60	78.05	76.88	79.36
X				X	60	78.05	77.03	79.65
	X	X			60	79.65	78.77	79.79
	X		X		60	80.81	78.34	80.81
	X			X	60	77.77	77.61	79.65
		X	X		60	80.09	78.19	79.36
		X		X	60	79.51	76.74	79.79
			X	X	60	78.63	77.47	79.65
X	X	X			90	80.96	78.34	79.50
X	X		X		90	80.67	78.63	78.92
X	X			X	90	78.49	78.19	79.36
X		X	X		90	80.38	78.19	79.50
X		X		X	90	78.92	76.59	78.63
X			X	X	90	79.51	77.32	80.23
	X	X	X		90	81.40	78.63	78.77
	X	X		X	90	80.96	78.34	79.94
	X		X	X	90	80.81	78.34	79.21
X	X	X	X		120	80.52	77.61	79.50
X	X		X	X	120	80.81	77.76	78.34
X	X			X	120	<b>81.69</b>	78.48	78.92
X	X			X	120	80.96	78.05	78.92
X		X	X	X	120	80.81	78.19	78.48
	X	X	X	X	120	80.52	77.90	78.05
X	X	X		X	150	80.38	77.47	78.34

We also analyzed the correlation between the statistical measures computed from the CNs to compose the feature vector. For this, the Pearson correlation coefficient was applied between the pairs of measures used to compose our feature vector. The Pearson coefficient quantifies the linear correlation between two variables, with values ranging from  $-1$  (for negative correlation) to  $1$  (for positive correlation) and  $0$  for no correlation. In our final feature vector, the statistical measures are computed from 30 sub-CNs that are modeled by 3 different radius ( $r = \{1, 2, 3\}$ ) and transformed by 10 threshold values, resulting in 30 features per measure. Thus, 30 correlation coefficients are obtained for each pair of measures. [Fig. 7](#) shows the Pearson coefficients estimated for the six pairs of measures used in the feature vector. As can be seen, there is a certain correlation between the features in some CNs (each feature represents a derived CN), which is expected because these parameters are estimated from the same histogram. However, note that there is a high correlation between the Mean and the other measures, and especially with the IDM. This correlation is also seen in the classification experiment in [Table 2](#).

#### 4.3. Comparison to other approaches

##### 4.3.1. Comparison to texture based analysis methods on the same data from OAI

In this section, our proposed approach is compared to texture based analysis methods for OA classification. We implemented four well known texture analysis methods: Gray Level Co-occurrence Matrix (GLCM) [29], fractal analysis [30], Local Binary Pattern (LBP) [31] and the Completed Local Binary Pattern (CLBP) approach [32]. The GLCM is a statistical technique that considers the spatial relationships of the gray-scale pixels for texture analysis [29]. This method computes the occurrence of two pixels according to a given difference in the gray intensity and a value of inter-sample spacing  $d$ . In this experiment, we adopted the distances  $(0, d)$ ,  $(-d, d)$ ,  $(d, 0)$  and  $(-d, -d)$ , two inter-sample spacings

(1 and 2) and the following GLCM features were evaluated using the cooccurrence matrix: contrast, correlation and homogeneity.

Fractal analysis is widely used for trabecular bone texture characterization [33–36]. In this study, we considered the method proposed by Backes et al. [30] which analyzes the complexity of the surface generated from a texture by applying the Bouligand-Minkowski fractal dimension [30]. The LBP [31] method is a popular texture descriptor that computes the frequency of local representations of texture. Each local representation is constructed by comparing each pixel with its neighborhood of pixels. We use the  $radius = 3$ ,  $neighbourhood = 24$  with uniform patterns that obtains 256 features. The CLBP [32] method is an extension of the traditional LBP. CLBP builds three operators (CLBP\_C, CLBP\_S and CLBP\_M) based on the local difference sign-magnitude transform of pixels. In our experiments, we used the joint 3D histogram (denoted as CLBP\_S/M/C),  $radius = 2$  and  $neighbourhood = 24$  with rotation invariant uniform patterns. The method produces a total of 648 features. The SVM classifier was retained for purpose classification. [Table 3](#) shows that the proposed method achieves the highest accuracy when compared to texture based analysis methods. Compared to the fractal method which achieved the highest accuracy among texture based methods, our proposed network increases the accuracy from 78.63% to 81.69%, which is significant in the context of knee OA prediction.

##### 4.3.2. Comparison to existing studies using same and different samples

In this section, our results are compared to existing studies. First on the same samples as ours from the OAI database [10,7,11]. Then to other published studies using OAI samples different from ours [8,9]. As can be seen in [Table 3](#), results show that our proposed method is competitive with the highest accuracy (81.69%), followed by the work of [8] (80.40%). Note that in [8], although the samples are from the same database, they are different and fewer. Woloszynski et al. [9] reached an accuracy of 78.80% with 137 X-ray images.

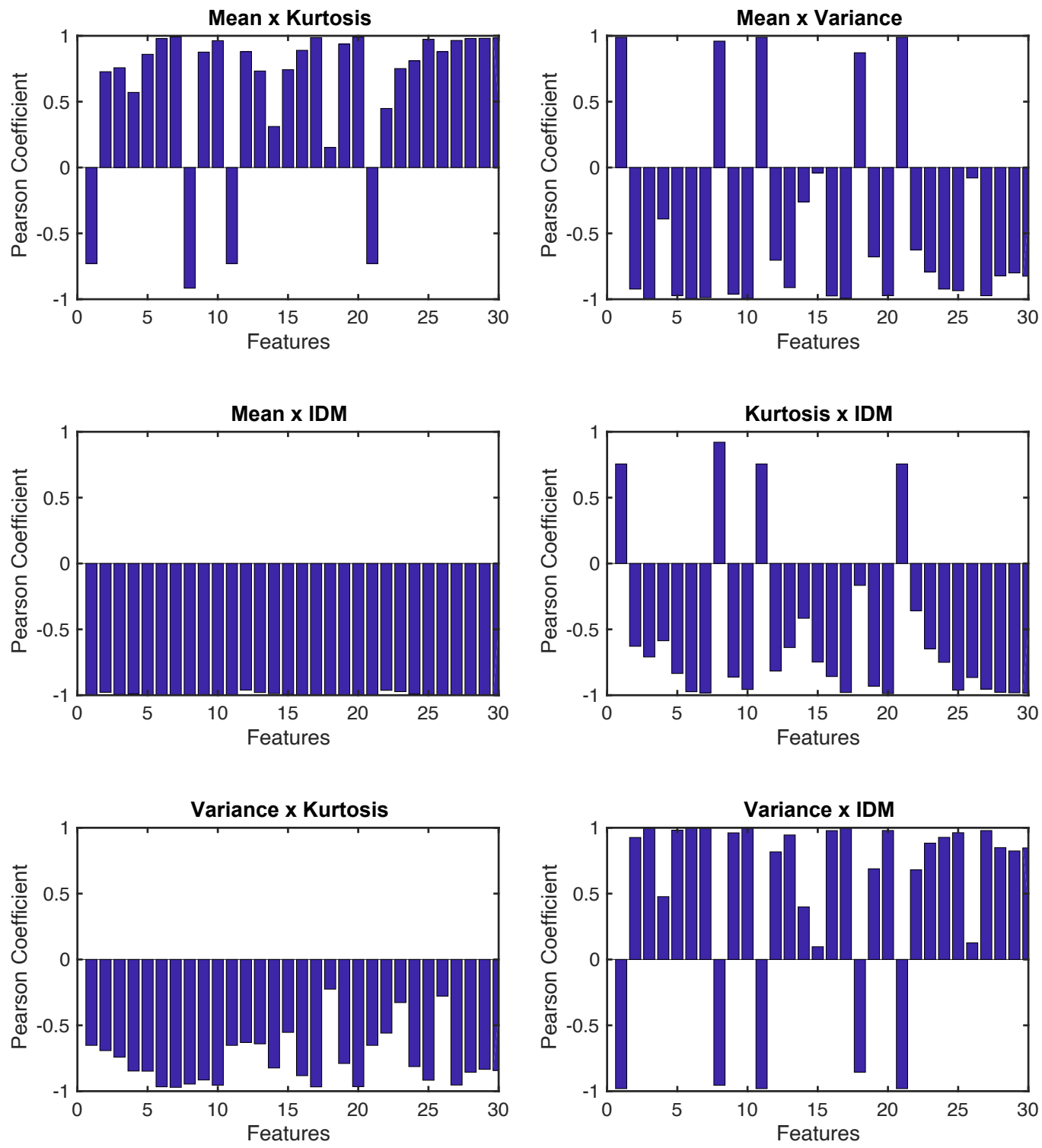


**Fig. 7.** Pearson correlation coefficients between pairs of measures used to compose the feature vector. For each pair of measures, the Pearson coefficient is computed for the 30 features obtained from the 30 sub-CNNs.

#### 4.4. Comparison to deep learning based models

##### 4.4.1. Comparison on the same samples from the OAI database

We also compared our approach to the following deep learning models: AlexNet [37], VGG-16 [38], GoogleNet [39], InceptionV3 [40], Resnet101 [41], Resnet50 [41], DenseNet201 [42] and EfficientNetb7 [43]. These learning models were used following two experiments.

*Experiment 1: Fine Tuning (FT)*

In this experiment, the initial weights learned from the ImageNet dataset were used to fine-tune each model. Then, the last fully-connected layers were replaced to correspond to our number of classes (CC & OP). We adopted the Adam optimization algorithm for training, 100 epochs, momentum 0.9, cross-entropy loss function, and learning rate 0.0001 for InceptionV3, Resnet50, Resnet101, and 0.00001 for AlexNet, GoogleNet, and VGG16. DenseNet201 and EfficientNetb7 were trained using the Adam optimization algorithm, 100 epochs, binary-

**Table 3**

The classification rates of the proposed method compared to existing studies in the literature.

	Method	No. of X-ray images	Sensitivity (%)	Specificity (%)	Accuracy (%)
Traditional descriptors	GLCM	688	79.36	75.00	77.18
	Fractals	688	82.85	74.42	78.63
	LBP	688	70.06	72.09	71.08
	CLBP	688	68.31	67.15	67.73
	Shamir et al. [8]	193	81.40	79.30	80.40
	Woloszynski et al. [9]	137	76.80	80.90	78.80
	Riad et al. [11]	688	85.47	75.29	80.38
Deep CNNs: Fine-Tuning	AlexNet	688	79.94	70.64	75.29
	VGG-16	688	73.98	71.22	73.98
	GoogleNet	688	78.20	72.38	75.29
	InceptionV3	688	78.20	67.15	72.67
	ResNet101	688	76.74	83.14	79.94
	ResNet50	688	74.71	77.32	76.02
	DenseNet201	688	94.48	62.79	78.63
	EfficientNetb7	688	53.20	97.96	75.62
Deep CNNs: GAP+SVM	AlexNet	688	79.07	69.19	74.13
	VGG-16	688	77.33	68.31	72.82
	GoogleNet	688	65.41	53.20	59.30
	InceptionV3	688	77.62	67.73	72.67
	ResNet101	688	65.70	63.37	64.53
	ResNet50	688	72.09	63.66	67.88
	DenseNet201	688	77.91	73.55	75.73
	EfficientNetb7	688	77.03	65.41	71.22
Other learning based studies	Antony et al. [14]	The whole OAI database	NA	NA	77.20
	Tiulpin et al. [16]	16384	NA	NA	79.65
	Nasser et al. [17]	2600	NA	NA	<b>82.53</b>
Proposed method	Complex Networks	688	77.62	85.75	<b>81.69</b>

entropy loss function and learning rates 0.001 and 0.0001 for DenseNet201 and EfficientNetb7, respectively.

#### Experiment 2: Global Average Pooling (GAP)

Here, the pre-trained weights from the ImageNet database were used to extract the features and the Global Average Pooling (GAP) over the feature maps of the last convolutional layer were used as descriptors.

For AlexNet, VGG-16, GoogleNet, InceptionV3, Resnet101, Resnet50, we used a 10-fold cross-validation scheme with 1-fold for testing, 1-fold for validation, and 8-folds for training; all folds were used for testing. These learning models were imported from Matlab 2018a and the images resized to  $224 \times 224$  pixels to feed the different learning models. For DenseNet201 and EfficientNetb7, we used a 1-fold scheme for testing and from the remainder folds, we defined 20% for validation and 80% for training. For these two models, we used the Keras 2.3 and TensorFlow 2.0 libraries in Python. For feature extraction (experiment 2), the descriptors computed from the learning models were evaluated with a leave-one-out cross-validation scheme along with the SVM classifier.

As can be seen on Table 3, in both experiments the proposed method achieved the highest accuracy compared to the other models. Obtained sensitivity and specificity using our approach are slightly lower than those obtained using DenseNet201 and EfficientNetb7 models, respectively. The highest accuracy, 79.94% achieved following ours, is reached by ResNet101. Note that in both experiments, when the selected deep learning models are fine-tuned (Experiment 1), better results are obtained compared to the feature extraction approach combining GAP and the SVM classifier (Experiment 2). Such behavior is expected because the deep learning models were pre-trained on the ImageNet dataset that is a domain unrelated to OA images. Thus, when using pre-trained models for feature extraction (Experiment 2), only more general characteristics are extracted from the images, such those related to shape and texture properties. In Experiment 1, fine-tuning the pre-trained models helps to learn from the images more specific characteristics related to OA and thus to improve the models for OA prediction.

#### 4.4.2. Comparison with existing studies using different samples from ours

In this section, our proposed complex network is compared to existing learning model approaches proposed in the literature for knee OA classification. Three studies were selected [14,16,17]. All were evaluated on data from the OAI database. Results reported here are collected from the papers. As can be seen in Table 3, the highest accuracy (82.53%) was achieved by the work of Nasser et al. [17] followed by our proposed method (81.69%). In [14,16], authors achieved an accuracy of 77.20% and 79.65%, respectively. As can be noticed, using a small number of samples (688 X-ray images) from a public database, our proposed approach obtains competitive accuracies compared to the literature for knee OA detection.

## 5. Discussion and conclusion

In this paper, using X-ray images, we have introduced a new approach based on complex networks modeling and statistical measurements for early knee OA detection. The proposed network approach enabled modelling the main characteristics of the X-ray images and increased the separation between control and OA groups. In terms of performance, compared to several methods of the literature, the proposed method achieved better scores in a detection task carried out over a challenging dataset from the OAI database.

Previous works have already shown the interest of texture analysis based methods [7–9,11] and model learning based methods [14,16,17] to separate OA progressors from non progressors. Janvier et al. [7] estimated the Hurst parameter H using fractal signature analysis, a quadratic variations estimator and the Whittle estimator. Combined to Joint Space Narrowing and clinical covariates, an AUC of 0.73 was reached. Shamir et al. [8] used different transform and texture analysis methods (Wavelets, Fourier, Chebyshev, Haralick) to extract different features. Using a dataset of 193 knee X-ray images, authors obtained an accuracy of 80.4% for classifying minimal OA (KL grade 2) from normal knees (KL grade 0). Woloszynski et al. [9] have investigated the ability of Signature Dissimilarity Measure (SDM) to predict OA progression over a 4-year period, authors reached an accuracy of 78.8% on a dataset

of 137 X-ray images. Riad et al. [11] used the Undecimated Dual Tree Complex Wavelet Transform (UDTCW) and the statistics of a new relative phase to extract new features related to OA. Using the SVM classifier and considering more neighbors in the relative phase they could reach an accuracy of 80.38% on a dataset of 688 knee X-ray images.

In regard to learning based methods for knee OA classification, Antony [14] et al. employed deep Convolutional Neural Networks (CNNs) to automatically detect knee joint regions and classify the different stages of knee OA severity. Using the whole OAI database, authors achieved an accuracy rate of 77.20%. Tiulpin et al. [16] proposed an approach based on Deep Siamese Convolutional Neural Network, which reduces the number of learnable parameters compared to standard CNNs. They used 16 384 knee X-ray images from the OAI database and obtained an accuracy of 79.65%. More recently, Yassine et al. [17] proposed a Discriminative Regularized Auto-Encoder (DRAE) based on Auto-Encoders. More specifically, authors combined a penalty term, called discriminative loss with the standard Auto-Encoder training criterion to force the learned representation to contain discriminative information about OA. Using the SVM classifier and 2600 knee X-ray images, an accuracy of 82.53% was reached.

### 5.1. Processing time analysis

Concerning the processing time for CNs computations, we used MATLAB R2017a and a system with an Intel (R) Core (TM) i7-3610QM CPU @ 2.30Ghz, 16 GB RAM, 64-bit Operating System. Our proposed method took on average 0.13 s for feature extraction from an image. On the other hand, the CLBP, Fractal, GLCM and LBP methods took on average 2.34 s, 0.97 s, 0.02 s and 0.004 s, respectively. These results show that the proposed method is also resource competitive, presenting a good trade-off between performance and processing time.

### 5.2. Strengths and limitations

This study has several important strengths. The database used is composed of 688 subjects with publicly available knee radiographs and grading (344 from control subjects and 344 from OA Patients). Both control and OA cases had KL = 0 at baseline. Thus, we believe that the findings of the proposed method are probably representative of early subchondral bone changes that happen before definite radiological OA detection on simple radiographs in the central compartment of the tibia. Also, this dataset had multicenter radiographs obtained using different devices. In other terms, the complex network was not tuned according to the equipment or to the clinical center. Thus, achieved predictions reflect the results of a multicenter cohort. In addition, the set of thresholds used for our proposed complex network is defined automatically.

This work has limitations that have to be considered. Only a region at the center of the subchondral bone was considered, it might be relevant to consider other regions from the central and medial regions of the tibia. Other regions can also be considered from the femoral bone, for which, at our knowledge, few studies have been devoted. This would be relevant to classify the patients into different groups (lateral/central/medial combined with tibial/femoral). Regarding Complex Network characterization, to overcome feature correlation and increase the accuracy, new ways to characterize the complex network can be considered. Complex network modeling can be studied further to improve the representation of knee OA patterns and to optimize the parameterization for OA prediction. We also believe that more sophisticated techniques based on complex networks can supply a better classification performance. Thus, this study opens a promising research field for knee OA prediction based on complex network models.

### CRediT authorship contribution statement

**Lucas C. Ribas:** Conceptualization, Software, Formal analysis,

Investigation, Validation, Writing - original draft, Writing - review & editing. **Rabia Riad:** Conceptualization, Data curation, Investigation, Methodology, Validation, Writing - original draft, Writing - review & editing. **Rachid Jennane:** Conceptualization, Data curation, Formal analysis, Methodology, Validation, Supervision, Project administration, Funding acquisition, Writing - original draft, Writing - review & editing. **Odemir M. Bruno:** Conceptualization, Methodology, Supervision, Resources, Project administration, Funding acquisition, Writing - original draft, Writing - review & editing.

### Declaration of Competing Interest

The authors declare that they have no known competing financial interests or personal relationships that could have appeared to influence the work reported in this paper.

### Acknowledgment

Authors gratefully acknowledge the financial support grant #2016/23763-8, São Paulo Research Foundation (FAPESP). Odemir Martinez Bruno gratefully acknowledges the financial support of CNPq (grant #307897/2018-4) and FAPESP (#2018/22214-6). We also gratefully acknowledge the French National Agency of Research (ANR) for its support through the ANR-20-CE45-0013-01 project. This manuscript was prepared using an OAI public use data set. The authors would like to thank the OAI study participants and clinical staff as well as the coordinating center at UCSF.

### References

- [1] C.J. Murray, J. Abraham, M.K. Ali, M. Alvarado, C. Atkinson, L.M. Baddour, D. H. Bartels, E.J. Benjamin, K. Bhalla, G. Birbeck, et al., The state of us health, 1990–2010: Burden of diseases, injuries, and risk factors, *JAMA* 310 (6) (2013) 591–606.
- [2] R.F. Loeser, S.R. Goldring, C.R. Scanzello, M.B. Goldring, *Osteoarthritis: A disease of the joint as an organ*, *Arthritis & Rheumatism* 64 (6) (2013) 1697–1707.
- [3] J.W. Bijlsma, F. Berenbaum, F.P. Lafeber, *Osteoarthritis: an update with relevance for clinical practice*, *The Lancet* 377 (9783) (2011) 2115–2126.
- [4] E. Lespessailles, R. Jennane, Assessment of bone mineral density and radiographic parameter texture at the tibial subchondral bone, *Osteoporosis International* 23 (2012) 871–876.
- [5] J. Kellgren, J. Lawrence, *Radiological assessment of osteo-arthritis*, *Annals of the Rheumatic Diseases* 16 (4) (1957) 494–502.
- [6] C. Buckland-Wright, Subchondral bone changes in hand and knee osteoarthritis detected by radiography, *Osteoarthritis and Cartilage* 12 (Supplement) (2004) 10–19, *The Role of Bone in the Treatment of Osteoarthritis: Proceedings of the 2001 Coral Gables Symposium*.
- [7] T. Janvier, R. Jennane, H. Toumi, E. Lespessailles, Subchondral tibial bone texture predicts the incidence of radiographic knee osteoarthritis: data from the osteoarthritis initiative, *Osteoarthritis and Cartilage* 25 (12) (2017) 2047–2054.
- [8] L. Shamir, S.M. Ling, W.W.S. Jr, A. Bos, N. Orlov, T.J. Macura, D.M. Eckley, L. Ferrucci, I.G. Goldberg, *Knee X-Ray image analysis method for automated detection of osteoarthritis*, *IEEE Transactions on Biomedical Engineering* 56 (2) (2009) 407–415.
- [9] T. Woloszynski, P. Podsiadlo, G.W. Stachowiak, M. Kurzynski, A signature dissimilarity measure for trabecular bone texture in knee radiographs, *Medical Physics* 37 (5) (2010) 2030–2042.
- [10] T. Janvier, R. Jennane, A. Valery, K. Harrar, M. Delplanque, C. Lelong, D. Loeuille, H. Toumi, E. Lespessailles, Subchondral tibial bone texture analysis predicts knee osteoarthritis progression: data from the osteoarthritis initiative: Tibial bone texture & knee OA progression, *Osteoarthritis and Cartilage* 25 (2) (2017) 259–266.
- [11] R. Riad, R. Jennane, A. Brahim, T. Janvier, H. Toumi, E. Lespessailles, Texture analysis using complex wavelet decomposition for knee osteoarthritis detection: Data from the osteoarthritis initiative, *Computers & Electrical Engineering* 68 (2018) 181–191.
- [12] W. Wang, D. Liang, Q. Chen, Y. Iwamoto, X.-H. Han, Q. Zhang, H. Hu, L. Lin, Y.-W. Chen, *Medical image classification using deep learning*, in: *Deep Learning in Healthcare*, Springer, 2020, pp. 33–51.
- [13] S. Rahman, L. Wang, C. Sun, L. Zhou, *Deep learning based HEP-2 image classification: A comprehensive review*, *Medical Image Analysis* 65 (2020), 101764.
- [14] J. Antony, K. McGuinness, N.E. O'Connor, K. Moran, *Quantifying radiographic knee osteoarthritis severity using deep convolutional neural networks*, in: *23rd International Conference on Pattern Recognition (ICPR)*, 2016, pp. 1195–1200.
- [15] J. Antony, K. McGuinness, K. Moran, N.E. O'Connor, *Automatic detection of knee joints and quantification of knee osteoarthritis severity using convolutional neural*

- networks, in: International Conference on Machine Learning and Data Mining in Pattern Recognition, Springer, 2017, pp. 376–390.
- [16] A. Tiulpin, J. Thevenot, E. Rahtu, P. Lehenkari, S. Saarakkala, Automatic knee osteoarthritis diagnosis from plain radiographs: a deep learning-based approach, *Scientific Reports* 8 (1) (2018) 1–10.
- [17] Y. Nasser, R. Jennane, A. Chetouani, E. Lespessailles, M.E. Hassouni, Discriminative regularized auto-encoder for early detection of knee osteoarthritis: Data from the osteoarthritis initiative, *IEEE Transactions on Medical Imaging* 39 (9) (2020) 2976–2984.
- [18] T. Chalumeau, L.d.F. Costa, O. Laligant, F. Meriaudeau, Texture discrimination using hierarchical complex networks., in: International Conference on Signal Image Technology and Internet based Systems (SITIS), Springer US, 2006, pp. 543–550.
- [19] L.C. Ribas, M.B. Neiva, O.M. Bruno, Distance transform network for shape analysis, *Information Sciences* 470 (2019) 28–42.
- [20] W.N. Gonçalves, B.B. Machado, O.M. Bruno, A complex network approach for dynamic texture recognition, *Neurocomputing* 153 (2015) 211–220.
- [21] A.R. Backes, D. Casanova, O.M. Bruno, Texture analysis and classification: A complex network-based approach, *Information Sciences* 219 (2013) 168–180.
- [22] A. Brahim, R. Jennane, R. Riad, T. Janvier, L. Khedher, H. Toumi, E. Lespessailles, A decision support tool for early detection of knee osteoarthritis using X-ray imaging and machine learning: Data from the osteoarthritis initiative, *Computerized Medical Imaging and Graphics* 73 (2019) 11–18.
- [23] OAI online, URL: <https://data-archive.nimh.nih.gov/oai/> (2018-11-14).
- [24] W.N. Gonçalves, B.B. Machado, O.M. Bruno, A complex network approach for dynamic texture recognition, *Neurocomputing* 153 (2015) 211–220.
- [25] L.C. Ribas, J.J.d.M.S. Junior, L.F. Scabini, O.M. Bruno, Fusion of complex networks and randomized neural networks for texture analysis, *Pattern Recognition* 103 (2020) 107189.
- [26] W.N. Gonçalves, A.R. Backes, A.S. Martinez, O.M. Bruno, Texture descriptor based on partially self-avoiding deterministic walker on networks, *Expert Systems with Applications* 39 (15) (2012) 11818–11829.
- [27] L.F. Scabini, D.O. Fistarol, S.V. Cantero, W.N. Gonçalves, B.B. Machado, J. Jose, F. Rodrigues, Angular descriptors of complex networks: A novel approach for boundary shape analysis, *Expert Systems with Applications* 89 (2017) 362–373.
- [28] G. Lester, The osteoarthritis initiative: A NIH public-private partnership, *HSS Journal* 8 (1) (2012) 62–63.
- [29] R.M. Haralick, Statistical and structural approaches to texture, *Proceedings of the IEEE* 67 (5) (1979) 786–804.
- [30] A.R. Backes, D. Casanova, O.M. Bruno, Plant leaf identification based on volumetric fractal dimension, *International Journal of Pattern Recognition and Artificial Intelligence* 23 (06) (2009) 1145–1160.
- [31] T. Ojala, M. Pietikäinen, T. Mäenpää, Multiresolution gray-scale and rotation invariant texture classification with local binary patterns, *IEEE Transactions on Pattern Analysis and Machine Intelligence* 24 (7) (2002) 971–987.
- [32] Z. Guo, L. Zhang, D. Zhang, A completed modeling of local binary pattern operator for texture classification, *IEEE Transactions on Image Processing* 19 (6) (2010) 1657–1663.
- [33] R. Jennane, R. Harba, G. Lemineur, S. Bretteil, A. Estrade, C.L. Benhamou, Estimation of the 3D self-similarity parameter of trabecular bone from its 2D projection, *Medical Image Analysis* 11 (1) (2007) 91–98.
- [34] R. Jennane, W.J. Ohley, S. Majumdar, G. Lemineur, Fractal analysis of bone X-ray tomographic microscopy projections, *IEEE Transactions on Medical Imaging* 20 (5) (2001) 443–449.
- [35] K. Harrar, R. Jennane, K. Zaouchi, T. Janvier, H. Toumi, E. Lespessailles, Oriented fractal analysis for improved bone microarchitecture characterization, *Biomedical Signal Processing and Control* 39 (2018) 474–485.
- [36] M.E. Hassouni, A. Tafraouti, H. Toumi, E. Lespessailles, R. Jennane, Fractional brownian motion and Rao geodesic distance for bone X-ray image characterization, *IEEE Journal of Biomedical and Health Informatics* 21 (5) (2017) 1347–1359.
- [37] A. Krizhevsky, I. Sutskever, G.E. Hinton, Imagenet classification with deep convolutional neural networks, *Advances in Neural Information Processing Systems* 25 (2012) 1097–1105.
- [38] K. Simonyan, A. Zisserman, Very deep convolutional networks for large-scale image recognition, *arXiv preprint arXiv:1409.1556*.
- [39] C. Szegedy, W. Liu, Y. Jia, P. Sermanet, S. Reed, D. Anguelov, D. Erhan, V. Vanhoucke, A. Rabinovich, Going deeper with convolutions, in: *The IEEE Conference on Computer Vision and Pattern Recognition (CVPR)*, 2015, pp. 1–9.
- [40] C. Szegedy, V. Vanhoucke, S. Ioffe, J. Shlens, Z. Wojna, Rethinking the inception architecture for computer vision, in: *The IEEE Conference on Computer Vision and Pattern Recognition (CVPR)*, 2016, pp. 2818–2826.
- [41] K. He, X. Zhang, S. Ren, J. Sun, Deep residual learning for image recognition, in: *The IEEE Conference on Computer Vision and Pattern Recognition (CVPR)*, 2016, pp. 770–778.
- [42] G. Huang, Z. Liu, L. Van Der Maaten, K.Q. Weinberger, Densely connected convolutional networks, in: *The IEEE Conference on Computer Vision and Pattern Recognition (CVPR)*, 2017, pp. 4700–4708.
- [43] M. Tan, Q. Le, Efficientnet: Rethinking model scaling for convolutional neural networks, in: *International Conference on Machine Learning*, PMLR, 2019, pp. 6105–6114.